Spin-charge separation in a 1D Fermi gas with tunable interactions

Ruwan Senaratne,[1,*] Danyel Cavazos-Cavazos,[1,*] Sheng Wang,[2,3] Feng He,[4] Ya-Ting Chang,[1] Aashish Kafle,[1] Han Pu,[1] Xi-Wen Guan,[2,5,†] and Randall G. Hulet[1,†]

[1] *Department of Physics and Astronomy, Rice University, Houston, Texas 77005, USA*
[2] *State Key Laboratory of Magnetic Resonance and Atomic and Molecular Physics, Wuhan Institute of Physics and Mathematics, APM, Chinese Academy of Sciences, Wuhan 430071, China*
[3] *University of Chinese Academy of Sciences, Beijing 100049, China*
[4] *SISSA and INFN, Sezione di Trieste, 34136 Trieste, Italy*
[5] *Department of Theoretical Physics, RSPE, Australian National University, Canberra ACT 0200, Australia*

(Dated: November 24, 2021)

Ultracold atoms confined to periodic potentials have proven to be a powerful tool for quantum simulation of complex many-body systems. We confine fermions to one-dimension to realize the Tomonaga-Luttinger liquid model describing the highly collective nature of their low-energy excitations. We use Bragg spectroscopy to directly excite either the spin or charge wave for various strength of repulsive interaction. We observe that the velocity of the spin and charge excitations shift in opposite directions with increasing interaction, a hallmark of spin-charge separation. The excitation spectra are in quantitative agreement with the Tomonaga-Luttinger liquid theory, and furthermore, we find that the spin excitations become dispersive at large interaction, signaling the onset of the nonlinear Luttinger liquid regime.

Unlike three-dimensional (3D) metals whose low-energy excitations are fermionic quasi-particles, the low-energy excitations of one-dimensional (1D) fermions are collective bosonic spin- and charge-density waves (SDW/CDW) that disperse linearly, as described by the Tomonaga-Luttinger liquid (TLL) theory [1–5]. Underlying this description is the remarkable result that the SDW and the CDW of an interacting 1D Fermi gas propagate at different speeds, thus causing a spatial separation of spin and charge.

Spin-charge separation has been studied in quasi-1D solid state materials by using momentum-resolved tunneling to determine the dispersions [6–8] and by angle-resolved photoemission spectroscopy [9–11]. A quantitative analysis of these data has proved challenging, however, because of the complexity of the electronic structure, and by the unavoidable presence of impurities and defects. Recently, a quantum gas microscope was employed in a series of related experiments with ultracold atoms on a single-site resolved 1D Hubbard chain leading to the observation of the fractionalization of spin and charge quantum numbers [12]; the modification of the SDW wavevector by density-doping and by spin-polarization [13]; and the study of simultaneous spin and charge dynamics resulting from a deconfinement-induced quench [14]. While related to the TLL theory, these experiments did not measure the collective low-energy excitation spectrum inherent to spin-charge separation. Separately exciting the spin and charge collective modes, as well as quantitatively determining their respective speeds as a function of interaction strength, have remained out of reach.

The excitation spectrum of the charge (density) mode of fermionic atoms confined to quasi-1D tubes has been previously measured for fixed interaction [15], and by us for variable interaction strength [16]. These experiments used two-photon stimulated Bragg spectroscopy, illustrated in Figs. 1A and 1B, to impart an observable momentum $\hbar q$, with energy $\hbar\omega$. The response of the 1D gas at a particular q and ω is related to the dynamic structure factor (DSF) $S(q,\omega)$, which characterizes the low-energy excitation spectrum for $q \ll k_F$, where k_F is the Fermi wave vector. At non-zero temperature, the Bragg response is proportional to $S(q,\omega) - S(-q,-\omega) = S(q,\omega)(1-\exp(-\hbar\omega/k_BT))$ [17, 18]. As depicted in Figs. 1C and 1D, the charge collective modes exhibit a particle-hole continuum and holon-antiholon pair

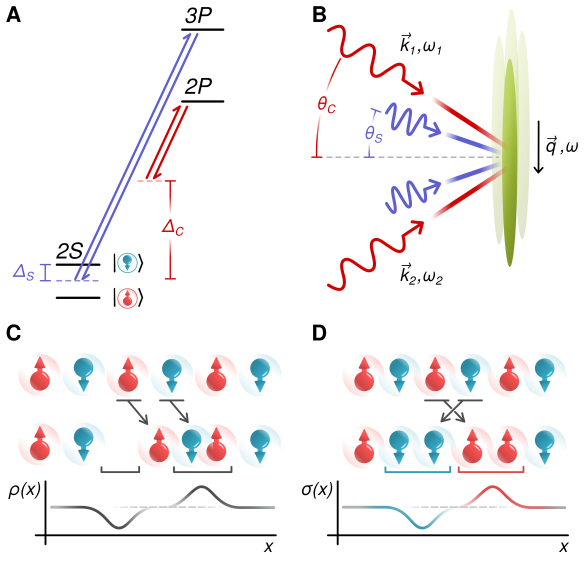

Fig. 1. Spin and charge excitations via Bragg spectroscopy. (**A**) Partial energy-level diagram of ^{6}Li showing relevant transitions and laser detunings for spin (Δ_S, violet) and charge (Δ_C, red) excitations. (**B**) Relative orientation ($\theta_{C,S}$) of each Bragg beam (1, 2) with respect to the axis perpendicular to the 1D tube direction . A momentum transfer $\vec{q} = \vec{k}_1 - \vec{k}_2 \approx 0.2\ k_F$ for the central tubes is delivered to the sample for a given relative detuning $\omega = \omega_1 - \omega_2$ between the beams. (**C** and **D**) Schematic diagram of the charge and spin excitations, showing an excitation of a holon-antiholon pair, or a spinon pair, respectively. The effect on the total density $\rho(x)$ and spin density $\sigma(x)$ is shown for each case at the bottom.

excitations, while the spin sector shows a two-spinon spectrum, which are the elementary spin excitations for the Yang-Gaudin model [19]. We can selectively excite either the SDW or the CDW depending on the detunings of the Bragg beams, as illustrated in Fig. 1A (see also [20]). In our previous work the charge-mode structure factor $S_C(q,\omega)$ was measured and quantitatively compared with Bethe ansatz theory, but we were unable to measure the spin-wave spectrum $S_S(q,\omega)$ due to spontaneous emission induced by the near-detuning of the Bragg pulse [16]. As described here, we have implemented improvements to our measurement method in order to reduce the spontaneous scattering rate to an acceptable level. In this report, we present measurements of both $S_C(q,\omega)$ and $S_S(q,\omega)$ as a function of the repulsive interaction strength. The measurements are then compared to Bethe ansatz and TLL theory, with the trapping potential taken into accout using the local density approximation (LDA), and for the first time, provide a quantitative test of spin-charge separation in the linear and nonlinear Luttinger liquid regimes.

A more detailed description of our experimental methods may be found in the supplementary materials [20]. We prepare a spin-balanced mixture of ^{6}Li atoms in the two energetically lowest hyperfine sublevels, states $|1\rangle$ and $|2\rangle$, and confine them in an isotropic optical trap. We evaporatively cool the atoms to a temperature $T \approx 0.1\,T_F$, where T_F is the Fermi temperature. Since a pure spin-wave is excited by tuning the Bragg beams evenly in-between the ground-state sublevels, we chose states $|1\rangle$ and $|3\rangle$ as our pseudo-spin-1/2 states, rather than $|1\rangle$ and $|2\rangle$ as used previously [16, 21], in order to maximize the detuning from the excited state and thus, to minimize the rate of spontaneous scattering. The frequency separation between the $|1\rangle$ and $|3\rangle$ states in the vicinity of the Feshbach resonance located at 690 G [22] is 159 MHz, compared with 78 MHz for the $|1\rangle$ - $|2\rangle$ combination. We use a radio-frequency π-pulse to drive the $|2\rangle \rightarrow |3\rangle$ transition at a magnetic field B corresponding to the desired value of a, the 3D s-wave scattering length. Following this process, we are unable to discern any residual population in state $|2\rangle$.

For the excitation of the SDW, we took the additional step of detuning the Bragg beams from the $3P_{3/2}$ excited state at a wavelength of 323 nm, rather than the usual 671 nm transition to the $2P_{3/2}$ state. The $3P_{3/2}$ state, which we use for Doppler cooling into the optical trap [23], has a linewidth that is nearly 8 times narrower than the $2P_{3/2}$ state. These two steps reduce the spontaneous scattering by more than a ten-fold factor for a given Bragg coupling, which is sufficient to measure $S_S(q,\omega)$.

We create an effectively 1D system by loading the atoms into a 2D optical lattice with depth $15\,E_r$, the recoil energy of a lattice photon of wavelength 1.064 μm. The resulting trap configuration is an array of quasi-1D tubes, which are tightly confined in the transverse dimensions (with trap frequency $\omega_r = 2\pi \times 225$ kHz), and are weakly harmonically confined in the axial dimension (with trap frequency $\omega_z = 2\pi \times 1.3$ kHz). The number of atoms per tube is non-uniform, and in general depends on the strength of interactions. In order to directly compare the DSFs obtained for different values of a, we use a repulsive green (532 nm) laser beam during the lattice ramp-up along each of the three orthogonal axes to compensate for variations in number per tube produced by the interaction. We measure the tube occupancy by taking *in situ* phase-contrast images of the atom cloud [24] and performing an inverse Abel transform to obtain the 3D distribution. A typical ensemble consists of a total of 6.5×10^4 atoms, has a peak tube occupancy of $\sim$50 atoms and a most probable tube occupancy of $\sim$30 atoms.

We perform Bragg spectroscopy by applying a pair of Bragg beams on the sample in a 200 μs pulse. We chose this time to minimize the pulse-time broadening while keeping the probe duration smaller than half the axial oscillation period. The wavelength of the Bragg beams are 671 nm and 323 nm for the charge- and the spin-mode measurements, respectively, and they are aligned with the angles $\theta_c \simeq 4.5^\circ$ and $\theta_s \simeq 2.2^\circ$ (Fig. 1B). In both cases the Bragg wave-vector has a magnitude $|\vec{q}| = 1.47\ \mu\mathrm{m}^{-1} \simeq 0.2\,k_F$ for a peak occupancy tube, and is parallel to the tube axis for both cases. We detune the charge-mode Bragg beams $\sim$11.4 GHz blue of the σ^+ D_2 transition. The detunings of the spin-mode Bragg beams from the π-transition to the $^3P_{3/2}$ manifold are of opposite sign for the two spin states and equal to half of the $\sim$159 MHz state-splitting in magnitude.

Because of this much smaller detuning, there is significantly more absorption of Bragg photons during the spin-mode Bragg pulse, which leads to atom loss. The intensity per beam is fixed to limit atom loss to 6-8% during the spin-mode measurement and to ensure that the momentum transfer is in the linear response regime for either mode over the entire range of interaction strengths we study [20]. There is no discernible atom loss during the charge-mode measurement. Immediately after the Bragg pulse, the atoms are released from the lattice, and are imaged using phase-contrast imaging following 150 μs of time-of-flight, after which atoms receiving the Bragg kick are clearly distinguished. We define the Bragg signal to be proportional to the number of out-coupled atoms [20].

Figure 2 shows the measured (symbols) and calculated (solid lines) Bragg spectra for both modes in the range of a from 0 to 500 a_0, where a_0 is the Bohr radius. Our DSF calculations take into account the effect of the inhomogeneous density due to the harmonic confinement along each tube. The strength of interactions is density dependent and is given by the dimensionless Lieb-Liniger parameter $\gamma = mg_1(a)/\hbar^2\rho_{1\mathrm{D}}$, where $g_1(a)$ is the coupling strength of the quasi-1D pseudopotential [25], and m is the atomic mass. The local density $\rho_{1\mathrm{D}}$ determines the local Fermi velocity and momentum (v_F and k_F). As the Bragg signal is proportional to the total transferred momentum, we sum up the local values of the DSF along each tube, by invoking the LDA to obtain the calculated spectra. Finally, we account for the frequency-broadening due to the finite duration of the Bragg pulses. A global temperature of 250 nK is the only free parameter in this model, other than scaling.

The value of $v_{c,s}/v_F$ for low-momentum excitations ($q \ll k_f$) can be computed as a function of γ via the Bethe ansatz[27, 28], which determines characteristic wavevectors $k_{c,s} = m^*(\gamma)v_{c,s}/\hbar$, where $m^*(\gamma)$ is the effective mass [20]. Knowledge of the local dispersion relation can be used to calculate a local value of $S(q,\omega)$ for both modes. While the dispersion relations $\omega_{c,s}(q)$ are linear for $q \ll k_{c,s}$, they acquire curvature outside of these regimes. Since k_c increases with increasing γ, we remain in the approximately linear TLL regime of the charge-mode for all interaction strengths probed, and the charge Bragg spectrum is essentially approximated by the imaginary part of the density-density correlation function for free fermions at low temperature. In contrast, k_s decreases rapidly with a larger γ, and thus our measurements of $S_S(q,\omega)$ increasingly probe the non-linear Luttinger liq-

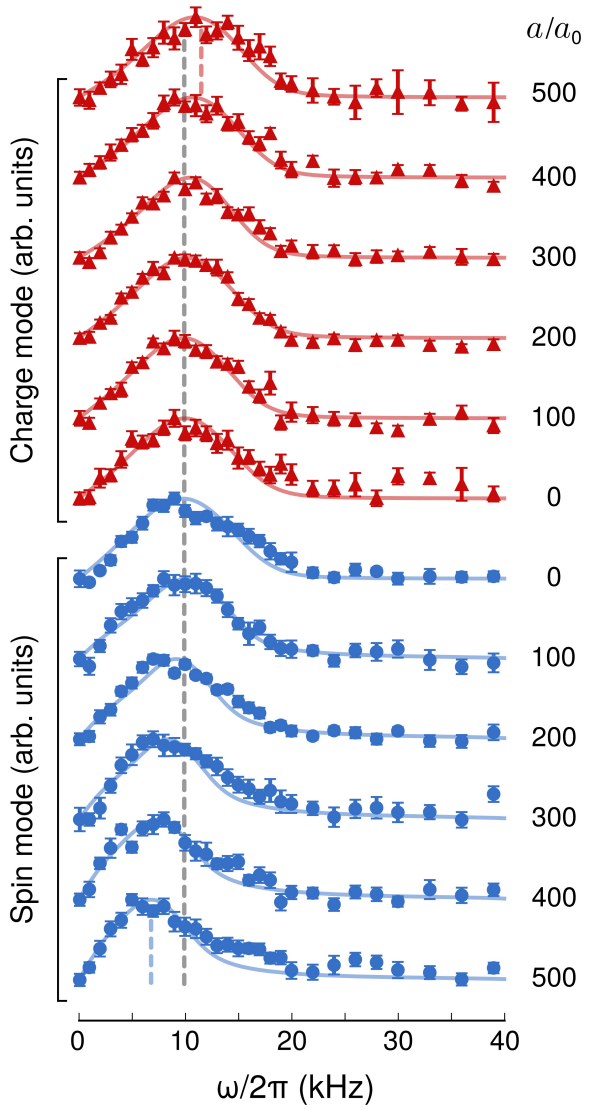

Fig. 2. Bragg spectra for $S_{C,S}(q,\omega)$. Normalized Bragg signals related to $S_C(q,\omega)$ (red triangles) and $S_S(q,\omega)$ (blue circles) for the range of 3D scattering length a from 0 to 500 a_0. Each data-point is the average of at least 20 separate experimental shots. Error bars represent standard error, obtained via bootstrapping [26]. Solid lines are the calculated Bragg spectra for a global temperature $T = 250$ nK with no additional fitting parameters other than overall scaling. Vertical dashed lines show the extracted peak frequency ω_p for the non-interacting case (gray), and the strongest probed interactions for the spin- and the charge-mode (blue and red, respectively).

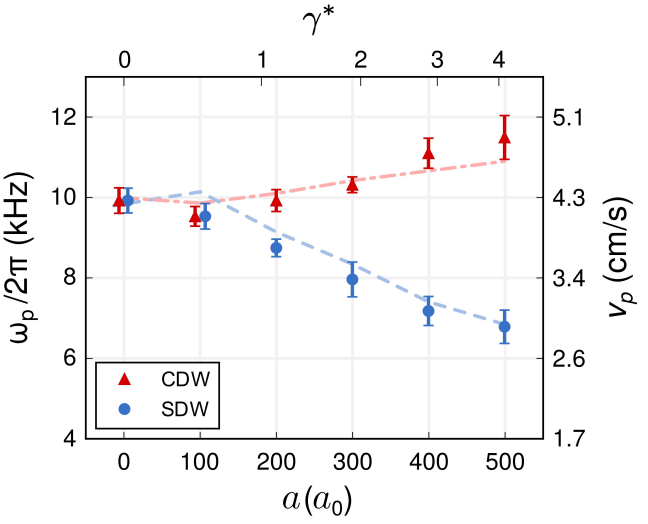

Fig. 3. Spin-charge separation. Peaks of measured Bragg spectra for charge (red triangles) and spin (blue circles) configurations for a ranging from 0 to 500 a_0. Peak frequency values determined via fits of a parabolic function to the data-points above 50% of the maximum measured value, and error bars are standard errors of the relevant fit parameters. The corresponding speed of sound $v_p = \omega_p/q$ is given by the right axis. The upper horizontal axis gives the interaction strength in terms of the Lieb-Liniger parameter γ^*, calculated for a median tube occupancy of 30 atoms. Lines show the calculated values for ω_p for the charge- and the spin-mode (dash-dotted red and dashed blue, respectively). Symbols for $a = 0$, 100 a_0 are slightly displaced from one another for clarity. We suspect that the nonmonotonic behavior shown by the calculated Bragg peaks for the spin mode at low interaction is due to the neglect of band curvature for the spin mode calculation.

uid (NLL) regime [29, 30]. The spin Bragg spectrum is thus subjected to the effects of back-scattering, and to higher order, those of band curvature and spin-charge coupling. Incorporating back-scattering into the linear TLL is sufficient to compute local values of $S_{C,S}(q,\omega)$ that agree with our data [20].

The frequency at which the Bragg signal reaches a maximum, ω_p, corresponds to the most probable value of the mode velocity, $v_p = \omega_p/q$, in the ensemble. We determine the peaks of each of the measured spectra by fitting a parabola to the data-points that are above 50% of the maximum measured value for each spectrum. The location of the peaks of the spectra obtained for our range of interaction are shown in Fig. 3, along with the peaks of the calculated spectra for each mode, which are in excellent agreement. In the non-interacting gas the spin and charge collective modes have the same speed, resulting in nearly identical measured spectra for the two cases. The congruence between the two spectra also confirms that the atom loss suffered during the spin-mode measurement is inconsequential. As the strength of the interaction is increased, the charge-mode velocity v_c increases, whereas the spin-mode velocity v_s decreases. This is seen in the shifts of the peaks of the two spectra: to a lower frequency for the spin-mode, and to a higher frequency for the charge-mode.

We further explored the NLL regime by extracting the axial width of the out-coupled atom packet after time-of-flight expansion. We show these widths in Fig. 4 as functions of interactions for both modes. As expected, the out-coupled widths increase with γ for measurements of the spin-mode, while remaining approximately constant for the charge-mode.

Bragg spectroscopy may be used to probe the ultracold-atom TLL beyond the demonstration of spin-charge separation contained in this work. Measurements with variable q can be conducted to further study the NLL and to benchmark novel calculations which include effects of band curvature and

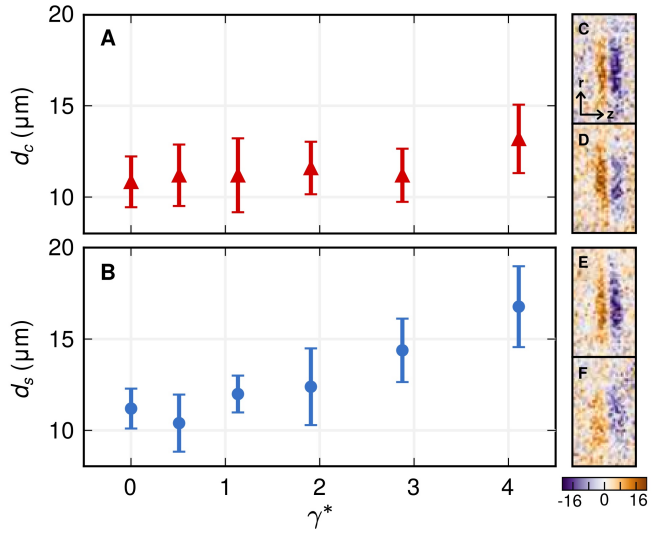

Fig. 4. Dispersion of spin and charge density waves. $1/e^2$ axial width following a Bragg pulse and 150 μs time-of-flight for (**A**) charge (d_c, red triangles) and (**B**) spin (d_s, blue circles) excitations, with a ranging from 0 to 500 a_0. The widths are the Gaussian fits to the postive outcoupled signal at ω_p. Error bars are standard errors determined by bootstrapping for at least 20 independent images [26]. The horizontal axis gives the Lieb-Liniger parameter γ^* calculated for a median tube occupancy of 30 atoms. (**C**-**F**) Representative samples of column density images of the atom cloud after a Bragg pulse. (**C**) Charge mode with $a = 0$ and (**D**) $a = 500\ a_0$. (**E**,**F**) Spin mode with $a = 0$ and $a = 500\ a_0$, respectively. Each frame corresponds to 40 μm x 65 μm.

spin-charge coupling [29, 30]. Additionally, at elevated temperatures and interactions, a spin-incoherent Luttinger liquid is expected, which supports a propagating charge-mode but not a spin-mode [31, 32]. Spin-imbalanced mixtures and attractive interactions are also of interest and are accessible via this technique. Experiments with shallower lattices will allow for the study of dimensionality effects due to tunneling between tubes [5]. It is increasingly clear that the oft-admired mathematical elegance of 1D many-body physics is well complemented by the purity and tunability of ultracold atoms.

* These authors contributed equally to this work.
† Corresponding author. Email: randy@rice.edu; xiwen.guan@anu.edu.au

[1] S.-I. Tomonaga, *Prog. Theor. Phys.* **5**, 544 (1950).
[2] J. Luttinger, *J. of Math. Phys.* **4**, 1154 (1963).
[3] F. Haldane, *J. Phys. C* **12**, 4791 (1979).
[4] J. Voit, *J. Phys.: Condens. Matter* **5**, 8305 (1993).
[5] T. Giamarchi, *Quantum Physics in One Dimension* (Oxford University Press, Oxford, 2003).
[6] O. Auslaender, *et al.*, *Science* **295**, 825 (2002).
[7] O. M. Auslaender, *et al.*, *Science* **308**, 88 (2005).
[8] Y. Jompol, *et al.*, *Science* **325**, 597 (2009).
[9] P. Segovia, D. Purdie, M. Hengsberger, Y. Baer, *Nature* **402**, 504 (1999).
[10] C. Kim, *et al.*, *Phys. Rev. Lett.* **77**, 4054 (1996).
[11] B. Kim, *et al.*, *Nat. Phys.* **2**, 397 (2006).
[12] T. A. Hilker, *et al.*, *Science* **357**, 484 (2017).
[13] G. Salomon, *et al.*, *Nature* **565**, 56 (2019).
[14] J. Vijayan, *et al.*, *Science* **367**, 186 (2020).
[15] G. Pagano, *et al.*, *Nat. Phys.* **10**, 198 (2014).
[16] T. L. Yang, *et al.*, *Phys. Rev. Lett.* **121**, 103001 (2018).
[17] A. Brunello, F. Dalfovo, L. Pitaevskii, S. Stringari, F. Zambelli, *Phys. Rev. A* **64**, 063614 (2001).
[18] P. Zou, E. D. Kuhnle, C. J. Vale, H. Hu, *Phys. Rev. A* **82**, 061605 (2010).
[19] F. He, *et al.*, *Phys. Rev. Lett.* **125**, 190401 (2020).
[20] See the supplementary materials .
[21] G. Veeravalli, E. Kuhnle, P. Dyke, C. Vale, *Phys. Rev. Lett.* **101**, 250403 (2008).
[22] G. Zürn, *et al.*, *Phys. Rev. Lett.* **110**, 135301 (2013).
[23] P. M. Duarte, *et al.*, *Phys. Rev. A* **84**, 061406 (2011).
[24] R. G. Hulet, J. H. V. Nguyen, R. Senaratne, *Rev. Sci. Instrum.* **91**, 011101 (2020).
[25] M. Olshanii, *Phys. Rev. Lett.* **81**, 938 (1998).
[26] B. Efron, *Ann. Statist.* **7**, 1 (1979).
[27] C. N. Yang, *Phys. Rev. Lett.* **19**, 1312 (1967).
[28] M. Gaudin, *Physics Letters A* **24**, 55 (1967).
[29] R. G. Pereira, E. Sela, *Phys. Rev. B* **82**, 115324 (2010).
[30] A. Imambekov, T. L. Schmidt, L. I. Glazman, *Rev. Mod. Phys.* **84**, 1253 (2012).
[31] G. A. Fiete, *Rev. Mod. Phys.* **79**, 801 (2007).
[32] P. Kakashvili, S. Bhongale, H. Pu, C. Bolech, *Phys. Rev. A* **78**, 041602 (2008).
[33] R. A. Hart, *et al.*, *Nature* **519**, 211 (2015).
[34] Y.-T. Chang, R. Senaratne, D. Cavazos-Cavazos, R. G. Hulet, *Phys. Rev. Lett.* **125**, 263402 (2020).
[35] D. Pines, *Theory of Quantum Liquids: Normal Fermi Liquids* (CRC Press, 2018).
[36] A. Imambekov, L. I. Glazman, *Science* **323**, 228 (2009).
[37] F. Haldane, *J. Phys. C* **14**, 2585 (1981).
[38] X.-W. Guan, M. T. Batchelor, C. Lee, *Rev. Mod. Phys.* **85**, 1633 (2013).
[39] A. Y. Cherny, J. Brand, *Phys. Rev. A* **73**, 023612 (2006).
[40] L. Balents, R. Egger, *Phys. Rev. B* **64**, 035310 (2001).
[41] M. Takahashi, *Progress of Theoretical Physics* **46**, 401 (1971).

ACKNOWLEDGMENTS

We would like to thank T. L. Yang for his contributions to the apparatus. **Funding:** This work was supported in part by the Army Research Office Multidisciplinary University Research Initiative (Grant No. W911NF-17-1- 0323), the NSF (Grant Nos. PHY-1707992 and PHY-2011829), and the Welch Foundation (Grant No. C-1133). H. P. acknowledges support from the U.S. NSF (PHY-1912068) and the Welch Foundation (Grant No. C-1669). X.W.G. is supported by the NSFC key grant No. 12134015, the NSFC grant No. 11874393, and the NKRDPC 2017YFA0304500. D.C.-C. acknowledges financial support from CONACyT (Mexico, Scholarship No. 472271). **Author contributions:** R.S and D C.-C. built the experimental setup, performed the measurements, and analyzed data. S.W. and F.H performed the modeling of the experimental data and the theoretical calculations. Y.C. and A.K. assisted with experiments. All work was supervised by H.P, X.W.G. and R.G.H. All authors discussed the results and contributed to the manuscript. **Compet-**

ing interests: The authors declare no competing interests. **Data and materials availability:** All data needed to evaluate the conclusions in the paper are present in the paper and the supplementary materials.

SUPPLEMENTARY MATERIALS

Materials and Methods

The apparatus and experimental procedures used to produce degenerate Fermi gases for this study have been discussed previously [16, 24, 33]. The primary differences with our previous experiment [16] are aimed at reducing spontaneous light scattering in the implementation of Bragg spectroscopy of the SDW. The sample is initially prepared in a spin-balanced mixture of the two lowest hyperfine sub-levels, which we label $|1\rangle$ and $|2\rangle$ respectively. At this stage, we trap 6.5×10^4 atoms in an isotropic harmonic trap with a geometric-mean trapping frequency of $(2\pi)\times$ 258 Hz produced by the intersection of three mutually-orthogonal focused trapping beams of wavelength 1.064 μm. Each beam is linearly polarized and initially retro-reflected with a perpendicular linear polarization in order to avoid lattice formation. The sample temperature is $0.1\,T_F$, where T_F is the Fermi temperature. We then transfer the state $|2\rangle$ atoms to the third highest hyperfine sub-level $|F = 3/2, m_F = -3/2\rangle$, which we label $|3\rangle$, by applying a π-pulse on the radio frequency magnetic dipole transition from $|2\rangle \rightarrow |3\rangle$. We tune the $|1\rangle - |3\rangle$ 3D s-wave scattering length, a, using a magnetic Feshbach resonance located at 690 G [22]. We perform the state transfer at the magnetic field corresponding to the desired value of a for each experimental run. The magnetic field is stabilized to $\pm$10 mG using a two-stage servo[34].

We then rotate the polarization of the retro-reflected beams by 90 degrees in order to form a shallow 3D lattice, and afterwards ramp up the intensities of the three trapping beams within 35 ms to reach a depth of 7 E_r along each axis, where $E_r = h\times$29.4 kHz is the recoil energy of a single trapping photon. We simultaneously turn on focused blue-detuned anti-trapping beams (532 nm) along each of the lattice axes. These 'compensation' beams are used to adjust the potential at the center of the trap, in order to achieve a consistent number profile across the ultimate ensemble of quasi-1D tubes across all studied interaction strengths[16].

Having loaded the atoms into the compensated 3D lattice, we ramp up the intensity of two of the trapping beams to reach a trapping depth of 15 E_r along two of the lattice axes in 20 ms, while simultaneously ramping the third beam and compensation beam intensities to zero. The resultant 2D lattice forms an array of quasi-1D tubes. Each tube has radial angular trapping frequency $\omega_r = 2\pi \times 227.5$ kHz and axial angular trapping frequency $\omega_z = 2\pi \times 1.34$ kHz, giving a tube aspect ratio ~170. We load an on-average spin-balanced sample of up to 60 atoms in each tube, with a temperature ~250 nK. Thus, the chemical potential $\mu \ll \hbar\omega_r$, and we avoid populating radially excited modes. The energy scale associated with tunneling between neighboring tubes is $\sim h \times 200$ Hz, and is much smaller than the thermal energy-scale, ensuring that the ensemble is 1D in nature [5].

Once the 2D lattice has been ramped up, we apply the Bragg pulse, by turning on the two Bragg beams for 200 μs. For the charge-mode measurement, each Bragg beam has a $1/e^2$ radius (waist) of 500 μm and a power of 200 μW. For the spin-mode, each Bragg beam has a waist of 100 μm and a power of 168 μW. The applied intensity I is significantly higher in the case of the spin-mode Bragg beams due to the poor UV transmission of the vacuum window used for this experiment, which we cannot directly measure but indirectly estimate to be ~10% via scattering rate measurements. For both modes we ensure that we are in the linear-response regime by varying I and checking that the measured Bragg signal size is proportional to I^2.

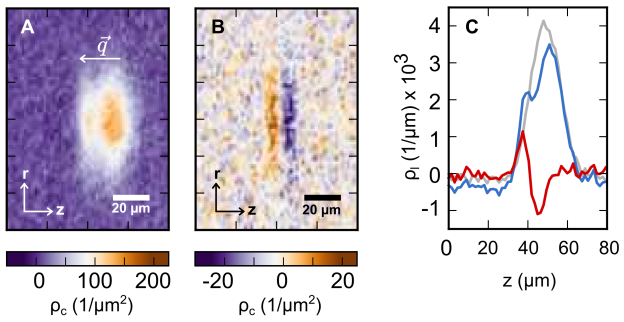

Fig. S1. Bragg signal extraction. (**A**) Column density (ρ_c) image of the atom cloud after a Bragg pulse delivers a momentum transfer $\vec{q}$ to the sample, and the sample is released from the trap and allowed to expand during a 150 μs time-of-flight. (**B**) Difference between (**A**) and a reference shot with no relative detuning between the Bragg beams. (**C**) Line density (ρ_l) of (**A**) and (**B**) (blue and red, respectively), and the reference shot (gray). Line densities are calculated by integrating the column density along r, the axis perpendicular to the 1D tube direction z. The Bragg signal is calculated as the sum of the absolute value of the offset-subtracted line densities.

At the end of the pulse, we turn off the lattice beams, and allow the atoms to expand freely for a further 150 μs, before imaging the cloud using polarization phase-contrast imaging (PPCI) [24]. We take images for varying values of the frequency difference between the Bragg beams. As shown in Fig. S1, an image of the outcoupled atoms is obtained by subtracting a reference image with $\omega = 0$, averaging over more than 20 independent experimental runs for both images. We sum the obtained difference image in the radial dimension, to obtain an axial line density which shows an excess of outcoupled atoms and a deficit at their origin. We subtract off any offset (which we determine by fitting), and then sum the absolute value of the line density to obtain the Bragg signal.

SUPPLEMENTARY TEXT

Controlling the number profile

The details of the number profile determine the ensemble dynamic structure factor (DSF), and thus the peak frequency of the measured Bragg spectrum. We measure the number profile in the 2D lattice using *in situ* PPCI, and performing the inverse Abel transform, which exploits the cylindrical symmetry of the array to obtain 3D densities. The measured number profile is an input into our calculations of the DSF and the expected Bragg spectrum. We ensure that the mea-

sured number profiles for all interaction strengths give a peak frequency of 10.0 ± 0.15 kHz in the calculated non-interacting Bragg spectrum. Thus, any shift in the peak frequency of the measured Bragg spectrum is due to the effect of interactions in 1D rather than systematic variation of the number profile.

In order to adjust the number profile, we tune the intensity of the compensation beams during the 3D lattice stage. We apply an anti-trapping potential of approximately $4\,E_r$ along each lattice axis for the non-interacting case in order to reduce the density at the center of the lattice. We use progressively less anti-trapping light for stronger repulsive interactions to achieve an equivalent number profile.

Effects of atom loss due to absorption of Bragg photons

Unlike in our measurements of the charge-mode Bragg spectrum, the absorption of Bragg photons during the spin-mode Bragg measurement is not negligible. Absorption events result in atom loss and occur at a rate $\propto I$, the intensity of the Bragg beams. We measured between $6-8\%$ loss during our spin-mode Bragg pulses. We determined that this atom loss does not have a significant impact on the measured spectra. Comparison between the charge-mode and spin-mode Bragg measurements for the non-interacting gas indicate that there is no detectable difference between the two spectra, as expected. Additionally, we took spin-mode Bragg spectra with various values of I in order to determine whether different levels of atom loss would affect the spectra. As expected, atom loss correlated with I, as shown in Fig. S2. By fitting the tails of the spectra to a Boltzmann exponential function we extracted an empirical temperature for each value of I and found no correlation with atom loss.

Charge and spin density wave excitations

If we consider a Fermi gas consisting of an equal number $(N/2)$ of spin-up ($\uparrow$) and spin-down ($\downarrow$) states, then the overall dynamic structure factor $S(q,\omega)$ (DSF) will have two independent components labeled by $S_{\uparrow\uparrow}$ and $S_{\uparrow\downarrow}$. We can then define a charge- and spin-density DSF given by [5]:

$$S_{C,S}(q,\omega) \equiv 2\left[S_{\uparrow\uparrow}(q,\omega) \pm S_{\uparrow\downarrow}(q,\omega)\right], \tag{1}$$

where the $+$ sign corresponds to charge and $-$ to spin, and each component is the Fourier transform of the density-density correlation function $G_{\sigma,\sigma'}(r,t)$ described by [35]:

$$G_{\sigma,\sigma'}(r,t) = \frac{1}{N}\langle \hat{\rho}_\sigma(r,t)\hat{\rho}_{\sigma'}(r,t)\rangle, \tag{2}$$

where $\hat{\rho}_\sigma(r,t)$ is the density operator for a spin state σ. At finite temperature, the momentum transfer to the system from the Bragg beams $P(q,\omega) \propto S(q,\omega)$, and using Fermi's golden rule we obtain:

$$P(q,\omega) \propto (R_\uparrow^2 + R_\downarrow^2)S_{\uparrow\uparrow} + 2R_\uparrow R_\downarrow S_{\uparrow\downarrow}, \tag{3}$$

where R_σ corresponds to the rate at which the system absorbs a Bragg photon. For our experimental conditions, $R_\sigma \propto 1/\Delta_\sigma$, where Δ_σ is the relative detuning of the Bragg beam with respect to each spin state. Thus, we can finally write:

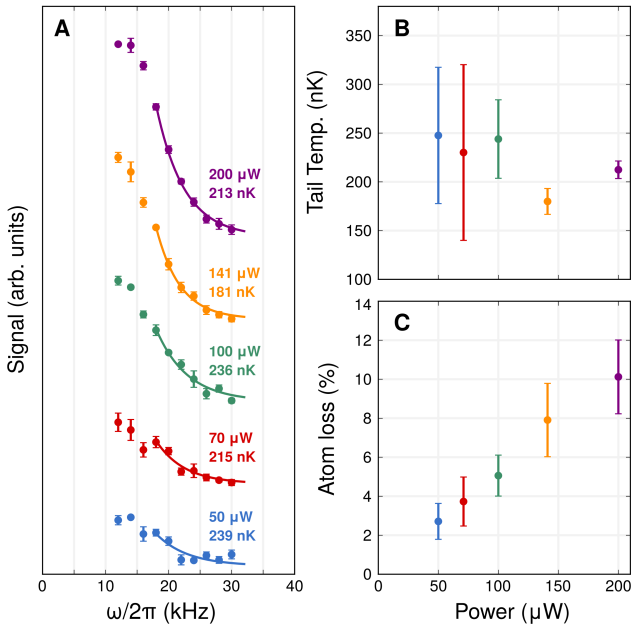

Fig. S2. Effects of atom loss on spin-mode Bragg spectrum. (**A**) Spin-mode Bragg spectra at 100 a_0 for high frequencies and various Bragg pulse powers (with fixed beam-waists). Fits are to $A\times\exp(-\hbar(\omega-\omega_c)/k_\mathrm{B}T)$ where A, ω_c and T are fit parameters and k_B is Boltzmann's constant. (**B**,**C**) Extracted temperature T from the fit and measured atom loss for several Bragg powers, respectively. Error bars correspond to the standard error of the mean.

$$P(q,\omega) \propto \left(\frac{1}{\Delta_\uparrow^2} + \frac{1}{\Delta_\downarrow^2}\right) S_{\uparrow\uparrow} + \frac{2}{\Delta_\uparrow\Delta_\downarrow} S_{\uparrow\downarrow}, \tag{4}$$

Equation 4 clearly shows that Bragg spectroscopy can provide independent access to the density and the spin DSFs by controlling the ratio between the detuning of the beams and the state-splitting of the two-level system. If the condition $\Delta_\uparrow \approx \Delta_\downarrow \gg \Delta_{\uparrow\downarrow}$ is satisfied, where $\Delta_{\uparrow\downarrow}$ is the state splitting, then $P(q,\omega) \propto S_C(q,\omega)$ and a charge-density wave is excited. On the other hand, if $\Delta_\uparrow = -\Delta_\downarrow$, then $P(q,\omega) \propto S_S(q,\omega)$ and the spin-density wave is excited.

Non-linear Luttinger Liquid

The Hamiltonian of the 1D δ-function interacting Fermi gas is given by

$$\mathcal{H} = -\frac{\hbar^2}{2m}\sum_{i=1}^{N}\frac{\partial^2}{\partial x_i^2} + 2c\sum_{1\le i<j\le N}\delta(x_i - x_j) - \mu N, \tag{5}$$

where N is the total number of particles, including $N_\uparrow$ spin-up fermions and $N_\downarrow$ spin-down fermions, and μ is the chemical potential. This is known as the Yang-Gaudin model and is Bethe ansatz solvable [27, 28]. In the above Hamiltonian, the coupling constant $c = -2\hbar^2/ma_{1\mathrm{D}}$ is determined by the effective 1D scattering length, given by $a_{1\mathrm{D}} = \left(-a_\perp^2/2a_s\right)\left[1 - C\,(a_s/a_\perp)\right]$[25]. In the following theoretical analysis we first take $\hbar = 1$, and $2m = 1$. Later we will recall their units for numerical simulation of charge and spin

dynamical structure factors. We define a dimensionless interaction strength $\gamma = c/n$ with n corresponding to the 1D density of the system for our later physical analysis. In this supplemental material, we consider repulsive interactions, i.e. $c > 0$.

Using the Bethe ansatz equations (BAE) given in [27], one can find distinct low-energy excitations [19] in the charge and spin sectors. As shown in Fig. S3, the charge sector has a particle-hole continuum spectrum, whose upper and lower bounds are given by

$$\omega(q) = v_c|q| \pm \frac{\hbar q^2}{2m^*} + \cdots, \tag{6}$$

showing a linear dispersion with quadratic curvature for arbitrarily strongly interacting fermions in the long-wave limit. In the above equation, v_c is the charge velocity and m^* is the effective mass, which can both be obtained from the BAE [19]. The low-energy spin excitation in the spin sector is also displayed in Fig. S3. It shows a typical two-spinon excitation spectrum, which are the elementary spin excitations for the Yang-Gaudin model [19]. For a small momentum q, the upper and lower bounds are given by

$$\omega_{s+}(q) = v_s|q| - \frac{v_s q^3}{2k_s^2} + \cdots, \qquad \omega_{s-}(q) = v_s|q| - \frac{2v_s q^3}{k_s^2} + \cdots, \tag{7}$$

respectively, where v_s is the spin velocity and k_s is the characteristic spin wavevector. The curvature leads to higher-order corrections in the nonlinear Tomonaga-Luttinger liquid [30, 36]. We observe that the upper boundary of the two-spinon excitation spectrum is determined by spinon particles, whereas the lower boundary is determined by two individual hole excitations.

In accordance with bosonization theory, one introduces charge and spin bosonic fields $\phi_{c,s} = (\phi_\uparrow \pm \phi_\downarrow)/\sqrt{2}$ and $\Pi_{c,s} = (\Pi_\uparrow \pm \Pi_\downarrow)/\sqrt{2}$. Here the fields ϕ_ν and their canonically conjugate momenta $\Pi_\nu = \partial_x \theta_\nu(x)/\pi$ obey the standard bosonic commutation relations, i.e. $[\phi_\nu, \Pi_\mu] = \mathrm{i}\delta_{\nu\mu}\delta(x-y)$ with $\nu, \mu = c, s$. For small momentum $q \ll k_F$, the 1D spin-1/2 repulsive Fermi gas can be described by an effective Hamiltonian [5, 30, 37]

$$H = H_c + H_s + \frac{2g_1}{(2\pi\alpha)^2}\int dx \cos(\sqrt{8}\phi_s). \tag{8}$$

The parameter α is a short-range cutoff. The first two terms describe the conventional linear TLL, i.e. the low-energy excitations of the 1D interacting Fermi gas separates into charge and spin collective bosonic modes, with

$$H_\nu = \int dx \left(\frac{\pi v_\nu K_\nu}{2}\Pi_\nu^2 + \frac{v_\nu}{2\pi K_\nu}(\partial_x \phi_\nu)^2\right). \tag{9}$$

This effective Hamiltonian characterizes the long-distance asymptotic decay of correlations in the 1D Fermi gas, i.e. the linear TLL behavior. The coefficients for different processes are given phenomenologically in [5]. The coefficient v_c/K_c is the energy cost for changing the particle density, while v_s/K_s determines the energy for creating a nonzero spin polarization. The last term in the effective Hamiltonian (8) characterizes the $2k_F$ back-scattering process, with $g_1 = c$ the coupling constant of this marginally irrelevant back-scattering operator. This back-scattering term only affects the spin sector, and as we will show, it has a quite significant effect on the spin DSF. In the above TLL description, the velocities $v_{c,s}$ and Luttinger liquid parameters $K_{c,s}$ can be calculated using the Bethe ansatz and thermodynamic equations [38]

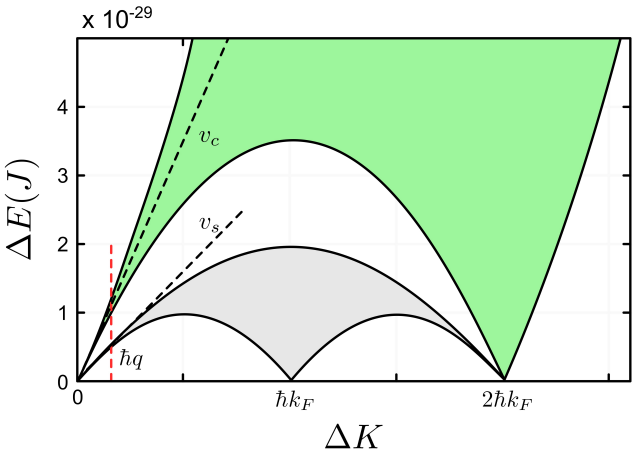

Fig. S3. Excitation Spectrum for Yang-Gaudin Model. Exact particle-hole (green) and two-spinon (gray) excitation spectra for repulsive Fermi gas at $\gamma = c/n = 5.03$ with the Fermi surface $k_F = n\pi$, where density $n = N/L = 3\times10^6$ (1/m), $\Delta E = \hbar\omega$. The black dashed line in the charge and spin excited spectrum corresponds to the charge velocity v_c and spin velocity v_s, respectively. Here the red dashed line shows the excited momentum imparted by the Bragg beams, which is set as $\Delta K = \hbar q$, $q = 1.47\ \mu m^{-1}$ for both charge and spin DSFs, respectively.

Charge and Spin DSFs

Although we have exact solutions of the model (Eq. (5)), the charge and spin dynamic structure factors for a repulsive Fermi gas have yet to be analytically calculated. This is a long standing theoretical challenge. From the TLL theory, at zero temperature, the charge DSF is a δ-function peak at $\omega = v_c q$ for $q \ll k_F$. As the leading correction to the linear dispersion for charge is quadratic in q, see Eq. (6), the charge DSF of a Fermi gas with finite repulsive interaction can be well approximated by that of a non-interacting ideal Fermi gas [29, 39]:

$$S(q,\omega) = \frac{\mathrm{Im}\chi(q,\omega,k_F,T,N)}{\pi(1-e^{-\beta\hbar\omega})}, \tag{10}$$

valid for $T \ll T_F = mv_F^2/2$ and $q \ll k_F$. The interaction effect can be accounted for by replacing k_F with $k_c = m^* v_c/\hbar$, as was done in previous work [16]. This DSF of the charge mode for free fermions gives us a good approximation of the charge excitation with dispersion given by Eq. (6).

For the spin DSF, we do not have a similar approximation in terms of non-interacting spinless fermions. At zero temperature, the spin DSF is a δ-function peak at $\omega = v_s q$. This will be broadened by band curvature and other irrelevant interactions that may lead to spin-charge coupling [29]. To calculate the contribution from these high order terms to the spin DSF remains extremely challenging, but they should scale as q^3. Hence, for $q \ll k_F$ and a temperature $T \sim v_s q \ll T_F = mv_F^2/2$, the elementary spin excitations are essentially captured by the effective Hamiltonian (8) which includes only the back-scattering term in addition to the linear TLL Hamiltonian.

At zero temperature, the back-scattering contributes to the spin DSF as a δ-function. At finite temperature, however,

such a δ-function peak is broadened. Therefore, the elementary excitations in the spin sector are bosons with finite lifetimes and the propagator of the dressed spin bosons is given by [29]

$$\widetilde{S}(q,i\omega)=\frac{1}{4\pi}\frac{q}{i\omega-v_sq-\sum(q,i\omega,T)}, \tag{11}$$

where $\sum(q,i\omega,T)$ is the self-energy of spin bosons, whose exact expression is very difficult to calculate. Here, based on Fermi's golden rule, we apply an approximate method to calculate the propagator in Eq. 11 [40]. We assume that the real part of the self-energy is zero (thus the mass shell of the spin boson is still $w=v_sq$), while the imaginary part is given by

$$\mathrm{Im}\sum\nolimits_q^{ret}=-\frac{1}{\tau_s(T)}=-\frac{\pi}{2}[g(T)]^2T. \tag{12}$$

where

$$g_1(T)\approx\frac{g(T)}{1+g(T)\ln(T_F/T)}, \tag{13}$$

is the renormalized coupling constant at finite termperature T and we use $g(T)=g_1(T)/(\pi v_s)$. We thus obtain the retarded spin-spin correlation function

$$\chi^{ret}(q,\omega)=-\frac{2K_s}{\pi}\frac{q}{\omega-v_sq+i/\tau_s(T)}, \tag{14}$$

the imaginary part of which leads to the spin DSF.

By comparing our calculations to our measured data, we determine that including the back-scattering term is necessary to model the spin Bragg spectra, particularly for large interactions (see Fig. S4). The linear TLL model fails to reproduce the observed high-frequency tails of the spin-mode Bragg spectra.

Computing the Ensemble DSF

In our experiment, we prepare the ultracold ^{6}Li gas in a 2D optical lattice, in which quasi-1D tubes are formed along the x direction. We apply the local density approximation (LDA) to treat physical quantities of the harmonically trapped 1D ultracold atomic system, where the density distribution satisfies the conditions

$$\begin{cases}\mu(n_{1D}(x))=\mu_0-V(x), & x\le R_F,\\ n_{1D}(x)=0, & x>R_F.\end{cases} \tag{15}$$

Here, R_F is Thomas-Fermi radius, $\mu(n_{1D}(x))$ is the effective local chemical potential and $V(x)=m\omega^2x^2/2$ is the trapping potential. In this case, the total number in the 1D tube is given by

$$N(\mu_0)=\int n_{1D}(\mu,x)\mathrm{d}x, \tag{16}$$

where the 1D density $n_{1D}(\mu,x)$ can be exactly calculated in terms of quasi-momentum density functions using the homogenous chemical potential μ_0 and the so-called Thermodynamic Bethe Ansatz (TBA) equations [41] .

For a given total number N in a 1D tube, one may obtain the density distribution along the tube direction by solving density functions and choosing a proper central chemical potential μ_0 in (15) to enforce Eq. (16). Furthermore, one may calculate the average DSF for a 1D tube via

$$S_{1D}(q,\omega,N)=\int S_0(q,\omega,n_{1D}(x))n_{1D}(x)\mathrm{d}x. \tag{17}$$

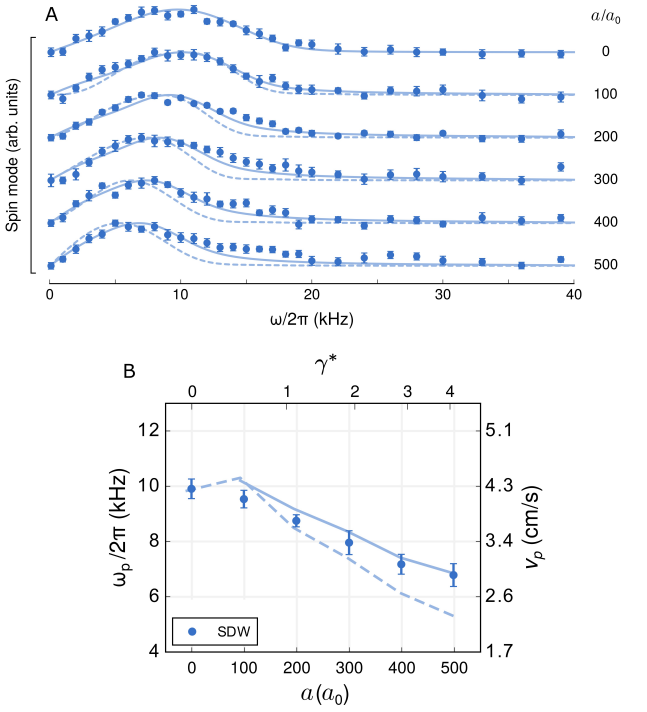

Fig. S4. Comparison of linear and nonlinear models. (**A**) normalized spin DSFs of repulsive Fermi gas with interactions in the range from 0 to 500 a_0. The symbols stand for experimental data. The solid lines are the results of assuming a finite temperature $T=250$ nK nonlinear Luttinger liquid which contains back-scattering, and the dashed lines are the results of assuming a linear Luttinger liquid. (**B**) Peak frequencies of theoretical and experimental spin DSF. We observe that for weak interactions, the theoretical peaks are larger than experimental ones, perhaps due to an inability to accurately model the contributions from the band curvature.

Thus, the total DSF of a 3D sample is given by

$$S_{3D}=\sum_i S_{1D}(q,\omega,N(r_i))N_t(r_i), \tag{18}$$

where $N(r_i)$ is the average particle number of each 1D tube at a radial distance r_i from the center of the array, i is the radial lattice index and $N_t(r_i)$ is the number of tubes at a distance r_i from the center.

The momentum transferred due to Bragg scattering is further broadened due to the finite duration of the Bragg pulse. We account for this broadening using [18]

$$\mathcal{P}(q,\omega)\propto\frac{1}{\pi\sigma}\int_{-\infty}^{\infty}\mathrm{d}\omega' S_{3D}(q,\omega')\mathrm{sinc}^2\left[\frac{\omega-\omega'}{\sigma}\right], \tag{19}$$

where $\mathrm{sinc}(x)=\sin(x)/x$ and the energy resolution $\sigma=2/\tau_{\mathrm{Br}}$ is set by the experimental Bragg pulse duration time $\tau_{\mathrm{Br}}=200\,\mu$s.